Seventh International Conference on Computational Fluid Dynamics (ICCFD7), Big Island, Hawaii, July 9-13, 2012

ICCFD7-3904

LES and PANS of passive and active control of flows around generic vehicle bodies

S. Krajnović and X. Han
Chalmers University of Technology, Gothenburg, Sweden, sinisa@chalmers.se

Abstract: The paper explores how time-dependent numerical techniques, large eddy simulation and Partially-Averaged Navier-Stokes, perform in predicting flow control of generic ground vehicles. Predictions of both passive and active flow control applications are explored. Passive flow control with cylindrical vortex generators was simulated for an Ahmed body with a slanted surface of 25^o at the rear end. Active flow control with periodic blowing and suction was applied at the end of a D-shaped body. Both the LES and the PANS were successful in predicting the flow control effect. The LES prediction of the flows around the Ahmed body was in better agreement with experimental observations than PANS. The PANS prediction of the active flow control of the D-shaped body was in good agreement with the LES prediction and the experimental observations. Furthermore, the PANS of the active flow control produced good results on a relatively coarse computational grid, showing the potential of the technique for flow control of higher Reynolds number flows.

Keywords: Flow control, LES, PANS, Active flow control, Vortex generators.

1 Introduction

The main contributor to the aerodynamic drag of ground vehicles is the low pressure on the rear end of vehicles caused by the wake region. The wake behind vehicles can be influenced by means of flow control which can be either passive using some add-on devices or active means such as blowing or suction. There are two main flow phenomena that should be influenced in order to change the wake and increase the pressure on the rear of the vehicle: the position of the separation and the shear layer instability. The separation of the boundary layer at the rear of the vehicle occurs either as a result of the geometry (sharp edge separation or sudden large change in the geometry at the rear end of the vehicle) or an adverse pressure gradient, which tends to decrease the motion of the boundary layer. One way of influencing the boundary layer separation is to produce streamwise vortices by for example vortex generators. The function of these longitudinal vortices is to sweep the high-energy air from the inviscid portion of the flow field or higher portion of the boundary layer to the inner parts of the boundary layer. As energy is added from the high-energy air to the retarded air inside the boundary layer, the separation is delayed, leading to an increased base pressure and lower drag of the train. The second flow phenomenon of interest is that, when the boundary layers on the surfaces of the vehicle separate at the rear end of the body, shear layers are formed that enclose the wake flow. These shear layers very quickly become unstable and start to interact with each other, resulting in vortex shedding. The shear layers are characterized by large energy dissipation that leads to a decrease in the pressure on the rear end surface. Interaction of the shear layers will in the time-averaged flow form a rather short separation bubble, producing low pressure on the rear end surface and thus high pressure drag. One way of influencing this process is to use periodic blowing and suction to delay the flow instabilities in the shear layers and thereby the shear layer interaction, and thus to make the mean separation bubble longer. This will redistribute the low pressure in the near wake and thus increase the rear end pressure and decrease the drag. Both of the flow strategies described above will be considered in the present work. Two flow cases documented in the literature are chosen for the purpose of the present numerical study. The passive flow control is the one described in the experimental work by Pujals et al. [1] where the large-coherent streaks

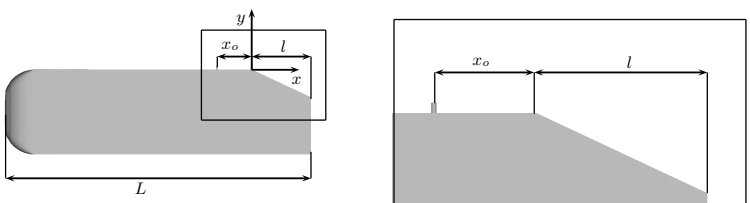

a) b)

Figure 1: a) Shape of the Ahmed body b) Zoom of the rear of the geometry.

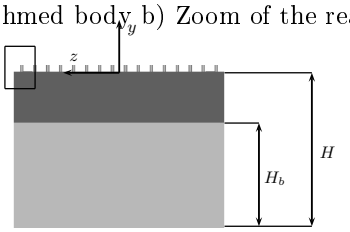

Figure 2: Ahmed body seen from behind.

are forced on the roof of an Ahmed body model. The active flow control study of a D-shaped body was described in the experimental work by Pastor et al. [2] and LES by Krajnović and Fernandes [3].

The paper presents numerical predictions of two flow-control processes for reduction of the aerodynamic drag of vehicle-like bluff bodies. Passive flow control by means of large-scale streamwise streaks is considered in the first part of the paper. An active flow control process using periodic blowing and suction is studied in the second part of the paper. Two time-dependent numerical techniques, large eddy simulation (LES) and Partially-Averaged Navier-Stokes (PANS), are used for the predictions, and the differences in the predictions are studied. Both flow cases are presented in section 2 and the numerical methods are described in section 3. Section 4 presents the results. Conclusions are given in section 5.

2 Description of the flow cases

2.1 Ahmed body with cylindrical roughness elements

The passive flow control case studied in the present work is that of the generic car model called the Ahmed body which has previously been studied in both experimental (e.g. Ahmed [4], Lienhart et al. [5]) and numerical work (Krajnović and Davidson [6, 7]). The geometry of the body and the computational domain are given in Fig. 1. All the geometric quantities are normalized with the body height, H, equal to 0.288 m. The values of the geometric quantities are $L/H = 3.625$, $l/H = 0.697$ and the width $W/H = 1.35$. The angle of the rear slanted surface was 25^o and the free-stream velocity was 20 m/s, resulting in the Reynolds number based on the model length L of $Re_L = 1.35 \times 10^6$. The geometry of the model is shown in Figs. 1 and 2. In a previous experimental study, Pujals et al. [1] used cylindrical roughness elements presented in Fig. 3 to force the large-scale streaks. They studied several configurations of the cylinders changing the height of the cylinders, k, their diameter, d, the spanwise spacing, λ_z, and the distance from the roughness to the rear slanted surface of the body, x_o. The experimental study by Pujals et al. [1] showed that the configuration of the roughness with 16 cylinders and $\lambda_z = 24$mm, $d = 6$mm, $k = 12$mm and $x_o = 120$mm resulted in a maximum drag reduction of approximately 10% . That configuration of the cylindrical roughness was chosen in the present study.

2.2 D-shaped body with active flow control

A sketch of the bluff body configuration is given in Fig. 4, which conforms with the experimental set-up [2, 8]. The body has the side shape of an Ahmed body with no slanted surface at the rear end. It extends from the one to the other lateral wall, forcing the fluid flows above and below it. It has a cross section with a chord length of $L = 262mm$, a height of $H = 72mm$ and a spanwise width of $W = 550mm$. The front of the body has a radius of $25mm$. Two trip tapes with a height of $0.8mm$ and length of $5mm$ were placed on

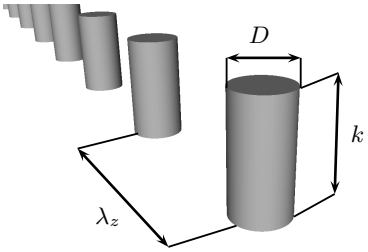

Figure 3: The relevant parameters of the cylindrical roughness elements.

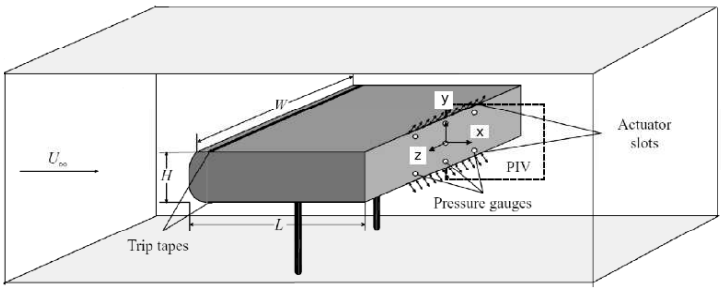

Figure 4: The geometry of the simplified vehicle model: quasi-2D Ahmed body, relevant notations and coordinate system, taken from [2].

the upper and the lower faces of the body $30mm$ downstream of the front. Based on the inlet velocity and the height of the model, the Reynolds number of the flow is $Re_H = 2.0 \times 10^4$.

3 Numerical methods and turbulence modelling

3.1 Partially-Averaged Navier-Stokes

Two of the most developed bridging methods are the Partially Integrated Transport Model (PITM) ([9]) and Partially-Averaged NAvier-Stokes (PANS) [10, 11]. The closure models forms in the two methods are similar but there are some differences. Partially-Averaged Navier-Stokes (PANS) is a method recently proposed by [10] as a bridging technique between RANS and DNS. The switch in PANS is continuous and based on the ratios of unresolved to total kinetic energy and dissipation.

The PANS equations ([11]) read:

$$\frac{\partial U_i}{\partial t} + U_j \frac{\partial U_i}{\partial x_j} + \frac{\partial \tau(V_i, V_j)}{\partial x_j} = -\frac{1}{\rho}\frac{\partial p}{\partial x_i} + \nu \frac{\partial^2 U_i}{\partial x_j \partial x_j}$$

Here a turbulent velocity V_i field is decomposed into two parts by an arbitrary filter as $V_i = U_i + u_i$. $\tau(V_i, V_j) = -2\nu_u S_{ij} + 2/3 k_u \delta_{ij}$ where k_u and ε_u are the unresolved trubulent kinetic energy, and the dissipation and the eddy viscosity of unresolved scales is given by [10] as

$$\nu_u = C_\mu \frac{k_u^2}{\varepsilon_u}$$

The resolved stress tensor is given by

$$S_{ij} = \frac{1}{2}\left(\frac{\partial U_i}{\partial x_j} + \frac{\partial U_j}{\partial x_i}\right)$$

The model equations for the unresolved kinetic energy k_u and the unresolved dissipation ε_u are required to

close the system of equation given previously. These equations as derived by Girimaji [11] are:

$$\frac{\partial k_u}{\partial t} + U_j \frac{\partial k_u}{\partial x_j} = P_u - \varepsilon_u + \frac{\partial}{\partial x_j}\left[\left(\nu + \frac{\nu_u}{\sigma_{ku}}\right)\frac{\partial k_u}{\partial x_j}\right]$$

$$\frac{\partial \varepsilon_u}{\partial t} + U_j \frac{\partial \varepsilon_u}{\partial x_j} = C_{\varepsilon 1} P_u \frac{\varepsilon_u}{k_u} - C^*_{\varepsilon 2}\frac{\varepsilon_u^2}{k_u} + \frac{\partial}{\partial x_j}\left[\left(\nu + \frac{\nu_u}{\sigma_{\varepsilon_u}}\right)\frac{\partial \varepsilon_u}{\partial x_j}\right] \tag{1}$$

Here, P_u and ε_u are the production and the dissipation rate of unresolved turbulent kinetic energy

$$P_u = -\tau(V_i, V_k)\frac{\partial U_i}{\partial x_k}$$

The model coefficients are

$$C^*_{\varepsilon 2} = C_{\varepsilon_1} + \frac{f_k}{f_\varepsilon}(C_{\varepsilon_2} - C_{\varepsilon_1}); \quad \sigma_{k_u} = \sigma_k \frac{f_k^2}{f_\varepsilon}; \quad \sigma_{\varepsilon_u} = \sigma_\varepsilon \frac{f_k^2}{f_\varepsilon}$$

where the unresolved to total ratio of kinetic energy and dissipation are written, respectively, as

$$f_k = \frac{k_u}{k}; \quad f_\varepsilon = \frac{\varepsilon_u}{\varepsilon}$$

The constant in the model depend on the chosen turbulence model. The unresolved-to-total-kinetic-energy ratio f_k in the original PANS model was prescribed as a constant. Following proposal of Girimaji and Abdol-Hamid [12], Basara [13] later modified the f_k to become a variable parameter that depends upon the grid spacing as follows

$$f_k \geq \frac{1}{\sqrt{c_\mu}}\left(\frac{\Delta}{\Lambda}\right)^{2/3}; \quad \Lambda = \frac{k^{3/2}}{\varepsilon} \tag{2}$$

k in Eq. 2 is computed as $k = k_r + k_u$ and

$$k_r = \frac{1}{2}\frac{\partial(U_i - \langle U_i\rangle_t)}{\partial x_i} \tag{3}$$

$\langle U_i\rangle_t$ is the averaged velocity.

An improved near-wall modeling in PANS was recently proposed by [14] in the form of the PANS $\zeta - f$ (also called PANS $k-\varepsilon-\zeta-f$) model. The PANS $\zeta-f$ model uses the four equation $k-\varepsilon-\zeta-f$ turbulence model proposed by Hanjalić et al. [15]. The $k-\varepsilon-\zeta-f$ model is derived from the $\bar{v}^2-f$ model [16] with a difference that a transport equation for wall normal velocity scale ζ ($=\bar{v}^2/k$, where k is turbulent kinetic energy) is used rather than the velocity scale $\bar{v}^2$. In this turbulence model, the $k-\varepsilon$ model is extended with an additional transport equation for the velocity scale ratio ζ and an equation for the elliptic relaxation function f for the purpose of improved near-wall behavior.

The PANS $\zeta - f$ model [14] is given by the following equations:

$$\nu_u = C_\mu \zeta_u \frac{k_u^2}{\varepsilon_u}$$

$$\frac{\partial k_u}{\partial t} + U_j \frac{\partial k_u}{\partial x_j} = P_u - \varepsilon_u + \frac{\partial}{\partial x_j}\left[\left(\nu + \frac{\nu_u}{\sigma_{ku}}\right)\frac{\partial k_u}{\partial x_j}\right]$$

$$\frac{\partial \varepsilon_u}{\partial t} + U_j \frac{\partial \varepsilon_u}{\partial x_j} = C_{\varepsilon 1} P_u \frac{\varepsilon_u}{k_u} - C^*_{\varepsilon 2}\frac{\varepsilon_u^2}{k_u} + \frac{\partial}{\partial x_j}\left[\left(\nu + \frac{\nu_u}{\sigma_{\varepsilon_u}}\right)\frac{\partial \varepsilon_u}{\partial x_j}\right] \tag{4}$$

$$C^*_{\varepsilon 2} = C_{\varepsilon 1} + f_k(C_{\varepsilon 2} - C_{\varepsilon 1})$$

$$\frac{\partial \zeta_u}{\partial t} + U_j \frac{\partial \zeta_u}{\partial x_j} = f_u - \frac{\zeta_u}{k_u} P_u + \frac{\zeta_u}{k_u} \varepsilon_u (1 - f_k) + \frac{\partial}{\partial x_j} \left[\left(\nu + \frac{\nu_u}{\sigma_{\zeta u}} \right) \frac{\partial \zeta_u}{\partial x_j} \right]$$

$$L_u^2 \nabla^2 f_u - f_u = \frac{1}{T_u} \left(c_1 + c_2 \frac{P_u}{\varepsilon_u} \right) \left(\zeta_u - \frac{2}{3} \right)$$

where constants C_μ, c_1, c_2 and $C_{\varepsilon 2}$ are equal to 0.22, 0.4, 0.65 and 1.9, respectively. L_u is the length scale and T_u is the time scale defined by using unresolved kinetic energy:

$$T_u = max \left[\frac{k_u}{\varepsilon}, C_\tau \left(\frac{\nu}{\varepsilon} \right)^{1/2} \right]; \quad L_u = C_L max \left[\frac{k_u^{3/2}}{\varepsilon}, C_\eta \left(\frac{\nu^3}{\varepsilon} \right)^{1/4} \right]$$

where constants C_L and C_τ are equal to 0.36 and 6.0, respectively. We assume that our numerical meshes support the cutoff in the energy containing scales and inertial range and choose $f_\varepsilon = 1$ (i.e. $\varepsilon_u = \varepsilon$). $C_{\varepsilon 1}$ is computed as $C_{\varepsilon 1} = 1.4(1 + 0.045/\sqrt{\zeta_u})$. This represents the four-equation PANS $\zeta - f$ model with enhanced near-wall attributes.

3.2 Large Eddy Simulation

The governing LES equations are the incompressible Navier-Stokes and the continuity equations filtered with the implicit spatial filter of characteristic width Δ. The filter width, Δ, is defined in this work as $\Delta = (\Delta_1 \Delta_2 \Delta_3)^{1/3}$, where Δ_i are the computational cell sizes in three coordinate directions. The algebraic eddy viscosity model originally proposed by [17] is used in this paper. The value of Smagorinsky constant $C_s = 0.1$ previously used for bluff-body flows [18], flow around a simplified bus [19] and generic car called Ahmed body [6] is used in this work. Using the Van Driest damping function $f = 1 - \exp(-n^+/25)$ (here, $n^+ = n u_\tau / \nu$), wall effects are partially taken into account by 'damping' length scale $l = C_s \Delta$ near the walls.

3.3 Numerical method

PANS and LES equations are discretized with a commercial finite volume solver, AVL FIRE, to solve the incompressible Navier-Stokes equations using a collocated grid arrangement. Convective fluxes are approximated by a blend of 95% central differences of second-order accuracy and of 5% upwind differences in LES and second-order upwind differences in PANS. The time integration is done using the second-order accurate three-time level Euler scheme. The same numerical discretization was previously used for LES of several bluff-body flows ([20],[21],[22],[23]).

3.4 Boundary conditions

3.4.1 Passive flow control boundary conditions

A uniform velocity profile, $U_\infty = 20$ m/s, constant in time was used as the inlet boundary condition for the Ahmed body flow in both PANS and LES. The values of k_u and ε_u on the inlet were set such that the ratio of the viscosity of the unresolved scales to the kinematic molecular viscosity is $\nu_u/\nu = 0.3$. The motivation for such a low value of ν_u comes from our previous numerical tests using PANS. The homogeneous Neumann boundary condition was used at the downstream boundary. The lateral surfaces and the ceiling were treated as slip surfaces. No-slip boundary conditions were used on the surface of the body and the channel floor.

3.4.2 Active flow control boundary conditions

The Reynolds number of the D-shaped flow based on the inlet velocity and the height of the model was $Re_H = 2 \times 10^3$ for the parametric study and $Re_H = 2 \times 10^4$ for the final case. A constant velocity profile was applied at the inlet, while the homogeneous Neumann boundary condition was used at the outlet. A no-slip boundary condition was applied on the surface of the body and on the upper, lower and lateral walls.

Harmonic actuation was applied to each slot by imposing a velocity on the boundary equal to $\vec{u}_s = u_A sin(\omega_A t)(cos(\phi)\vec{i} + sin(\phi)\vec{j})$, where $\vec{i}$ and $\vec{j}$ are the unit vectors in the x and y directions, respectively,

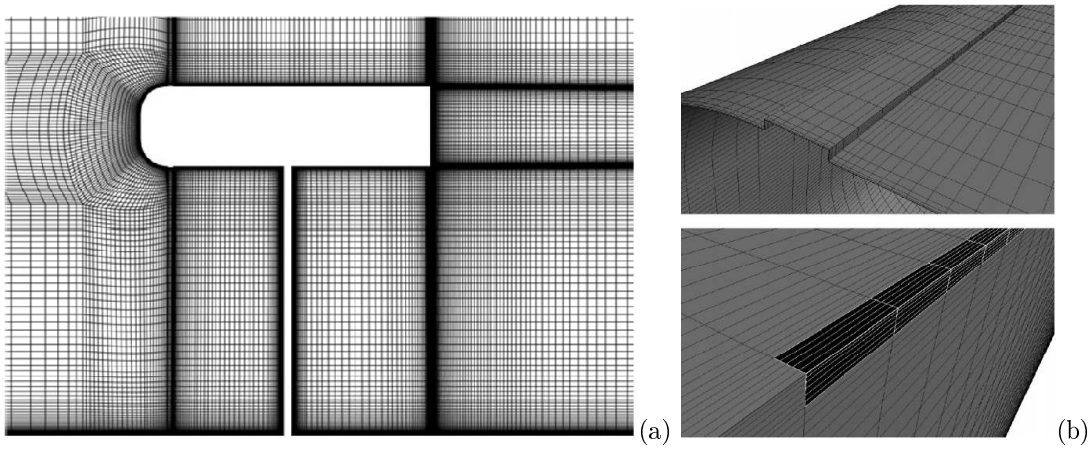

Figure 5: The computational mesh: (a) side view, (b)zoom of the trip tape and the actuation slot

and the actuation angle, ϕ, was 45^o, in agreement with the experiments. The actuation amplitude, u_A, can be derived from the expression for the momentum coefficient, $C_\mu = 4su_A^2/HU_\infty$. The actuation frequency and the moment coefficients in the present study were $St_A = 0.17$ and $C_\mu = 0.015$, respectively.

3.4.3 Computational grids and the resolution of the flow

Computational grids were made using a ICEM-CFD grid generator. Accuracy was established by making simulations on several different multi-block hexahedral conforming computational grids.

The computational grids used for the passive flow control of the Ahmed body flow were different for the natural and the controlled flows. For the natural flow, a computational grid of approximately 16 million computational cells was used. Two different computational grids were used for the flow with cylindrical roughness, containing approximately 18 and 30 million cells. The wall normal resolution of all computational grids was below $y^+ = 1$. The resolution in the streamwise direction varied between 50 and 250 wall units. The spanwise resolution was between approximately 30 and 80 wall units with a wide spread for the controlled flow due to the presence of the cylinders. As results below show, there is still room for improvement of the resolution of this flow. Krajnović [24] showed that the LES of the flow around a finite circular cylinder requires very fine computational grids, and having 16 cylinders in the present configuration the well resolved LES of this flow will require much more than the 30 million cells used in the present simulation. The resolution requirements of this flow remain to be investigated in the future.

Three computational grids containing 3.5, 5.5 and 7.5 million nodes were used for the D-shaped body with active flow control. A grid topology was constructed using several O and C grids in order to concentrate most of the computational cells close to the body. An example of the grid used for the D-shaped body is shown in Fig. 5. The same computational grids were used for the natural and the controlled flows of the D-shaped body flows. The resolution in the wall-normal direction was less than $y^+ = 1$. The resolution in the streamwise and the spanwise directions was around 14 and 30 wall units, respectively, in the LES on the medium computational grid. Similar values were obtained for the PANS simulations. It is important to keep in mind that the resolution of the controlled case was worse, as the blowing at the rear end increased the local velocity of the flow, while the computational grid was unchanged.

The time step in all simulations was chosen such to allow for a CFL number lower than 1 in more than 99% of the computation cells during entire simulation time.

4 Results

The comparison of the predictions between the LES and the PANS is first presented. This is followed by the exploration of the flow control mechanisms and their influence on the flow from the results of the LES.

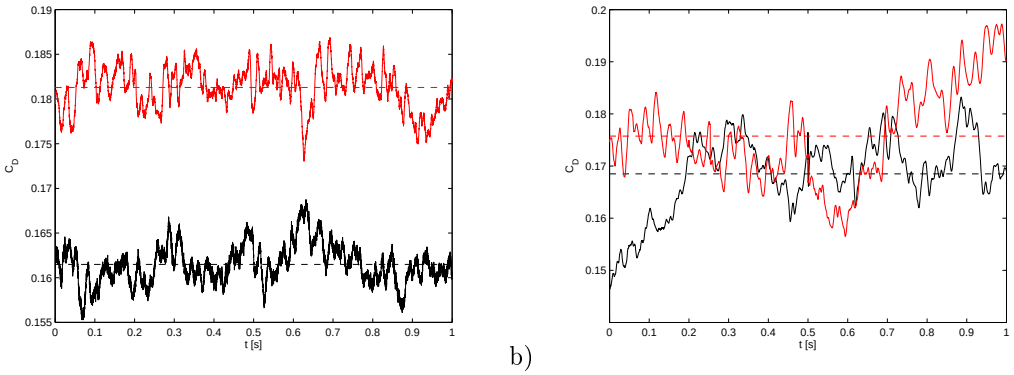

Figure 6: Comparison of the drag coefficient between the natural (red curve) and actuated flows (black curve) for a) LES and b) PANS.

4.1 Influence of the flow control on drag

The drag reduction as a result of the passive flow control applied on the Ahmed body is quantified in the present work by ΔC_d, defined as $\Delta C_d = 2\frac{C_d C_d^o}{C_d + C_d^o}$, where C_d^o and C_d are the time-averaged drag coefficients of the natural and controlled flow, respectively. The same quantity was computed in the experimental work by Pujals et al. [1]. The time histories of the drag coefficients for the LES and the PANS predictions are presented in Fig. 6. Both the absolute values of the drag coefficients and the difference between the natural and the controlled flows coefficients is different between the LES and the PANS. We find that $\Delta C_d^{LES} = 11.7\%$ and $\Delta C_d^{PANS} = 4\%$. The value obtained in the experiments by Pujals et al. [1] was around $\Delta C_d^{EXP} = 10\%$ which is close to the present LES prediction. Unfortunately, no absolute values of the drag coefficients are reported for this Reynolds number, and therefore only the drag reduction coefficient is compared between the experimental and the numerical studies. The prediction of the flow around an Ahmed body with an angle of the rear slanted surface of 25^o has earlier been studied using various numerical techniques such as steady and unsteady RANS, detached eddy simulations (DES), PANS and LES. The flow produced by this geometry is known to contain a high level of unsteadiness above the rear slanted surface, resulting in high levels of turbulent kinetic energy. The flow that separated at the start of the slanted surface later reattaches on the slanted surface, and this feature has proven to be difficult to predict with all the numerical techniques described above except the LES. The reason for the failure in the prediction of this flow with RANS or hybrid techniques such as DES is found in inadequacy of the turbulence modeling to deal with the complicated flow process in the separated wake flow of the body. Although the initial PANS (using $k-\varepsilon$ turbulence model) prediction by Basara et al. [13] showed a better prediction of the flow than previous DES or RANS, the differences between the PANS flow and the experiments were still significant. The present PANS predictions, although using a different RANS model ($\zeta - f$) as a basis, are no exception and prove that the RANS near-wall modeling of this flow is probably not a good idea.

Figure 7 shows comparisons of the LES and the PANS predictions of the flow around the rear end of the Ahmed body. As in the previous prediction at different Reynolds number, the present LES produced a reattachment of the flow on the rear slanted surface in the natural flow (Fig. 7a). The PANS on the other hand resulted in a large separation bubble on the slanted surface that covers the entire length of the slant. Thus the PANS prediction is different from the experimental observations and further usage of PANS for prediction of the flow change on the slanted surface with flow control is not trustworthy. Figure 7d shows that the separation bubble on the slanted surface becomes thinner in the PANS prediction of the actuated flow. As a result of that, the angle of the flow falling down above the slanted surface in the near wake is changed and the near wake is elongated. This is the same phenomenon as observed in the experimental investigation by Pujals et al. [1] but the position and size of the flow structures in the experiments were different from those in the PANS observations. The LES prediction of the actuated flow shown in Fig. 7b produces a much thinner separation bubble on the slanted surface, and the near-wake separation bubble is elongated. This is the desired consequence of the flow control strategy applied here, as an elongated near-wake separation

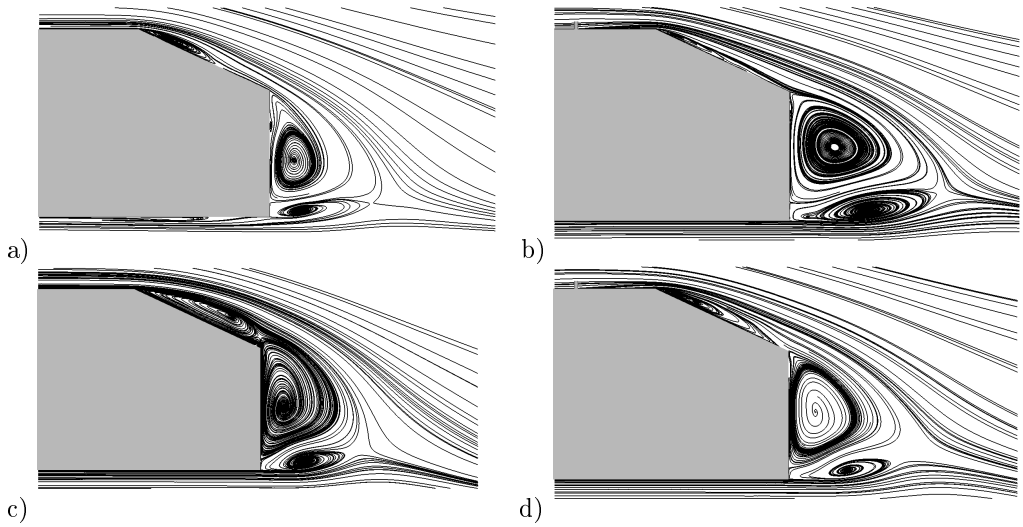

Figure 7: Streamlines projected onto the symmetry plane: a) LES natural flow b) LES controlled flow, c) PANS natural flow and d) PANS controlled flow.

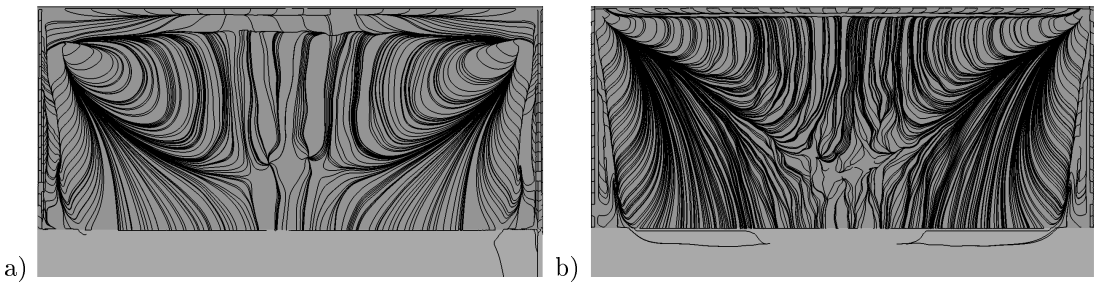

Figure 8: Particle traces on the rear slanted surface from the present LES: a) natural flow b) controlled flow.

bubble results in higher surface pressure on the vertical base of the Ahmed body.

The predicted LES particle traces on the rear slanted surface are shown in Fig. 8 for the natural and the controlled flows. As known from previous experimental observations and LES predictions, the main flow features consist of the trailing vortices and the separation bubble on the slanted surface. The imprint of these flow structures is visible in both the natural and the controlled flows with differences in sizes and positions. Krajnović and Davidson [7] showed that the separation bubble on the slanted surface has another very thin separation region just under it directly after the sharp edge between the roof and the slanted surface. The two parallel lines (so called bifurcation lines) below the upper sharp edge in Fig. 8a indicate the location of this structure in the natural flow. This region is considerably reduced in the actuated flow in Fig. 8b. Furthermore, the imprint of the main separation region on the slanted surface has a more triangular shape in the controlled flow as compared to a more half-circular shape in the natural flow. The experimental observation by Pujals et al. [1] showed that this separation bubble is perhaps even more suppressed, and it is hardly visible in their observations. It is possible that the actuated flow in the present LES is not fully resolved and that further refinement of the computational resolution is required for final conclusions about the flow structures in the actuated flow.

Pujals et al. [1] used the near-wall PIV to measure the flow in a plane located 1 mm from the slanted surface. The velocity field from their measurements is compared with the results of the present LES in Fig. 9. Note, however, that the legend scale in the experiments and the LES is not identical. The experimental figures show the recirculation bubble in the natural flow. The control flow in the experiments does not show any backflow in Fig. 9b indicating that the recirculation bubble is suppressed in the experiment. The natural flow in the present LES (Fig. 9c) is in good agreement with the natural flow in the experiment. The flow resulting from the LES of the controlled flow shows a clear region of backflow (although smaller than in the

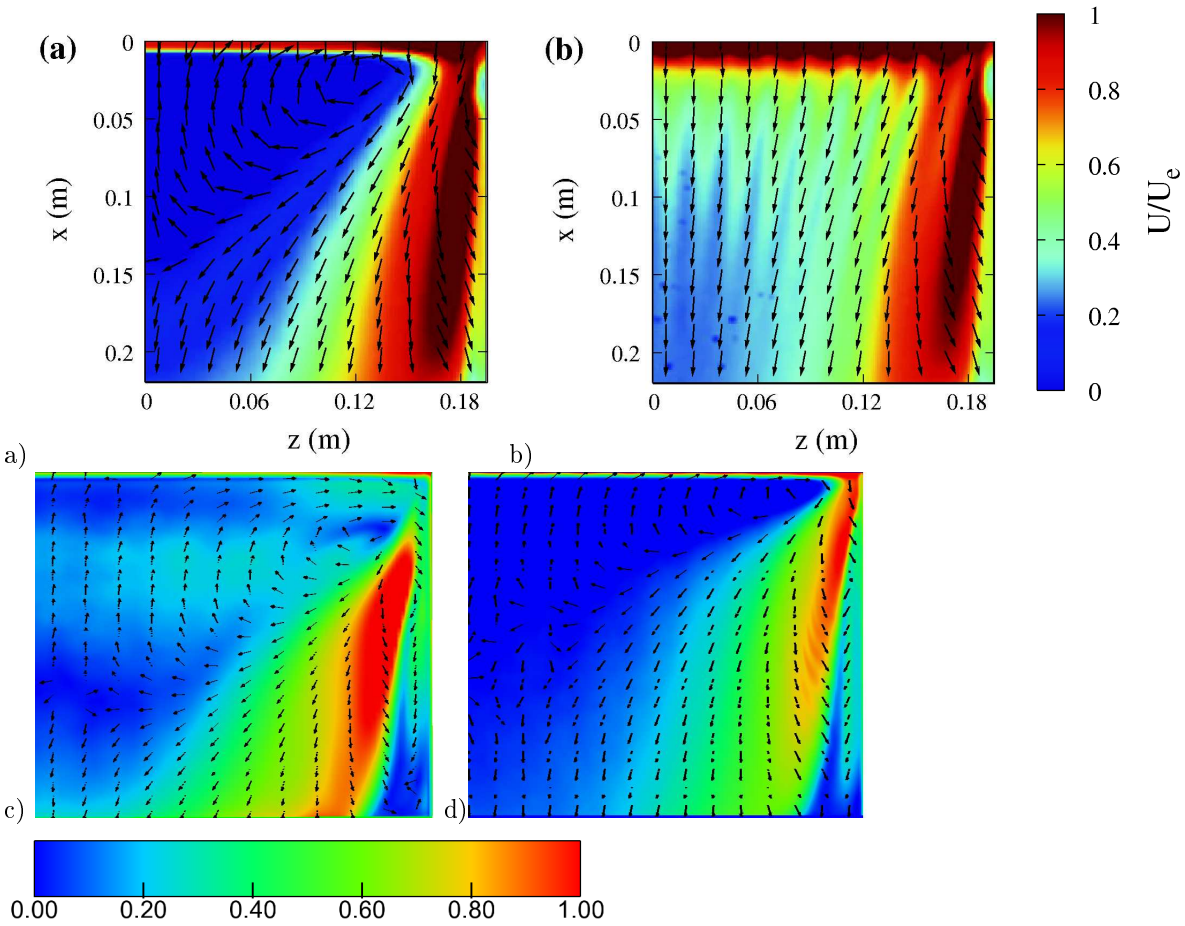

Figure 9: Time-averaged streamline velocity at $Y/k = 0.08$ above the slanted surface. The flow is from top to bottom. The surface is colored with U/U_∞ (U_∞ is denoted U_e in the experimental label). Note that the color scale is not identical in the LES and the experiments. a) Natural flow (experiment), b) controlled flow (experiment), c) natural flow (LES) and d) controlled flow (LES)

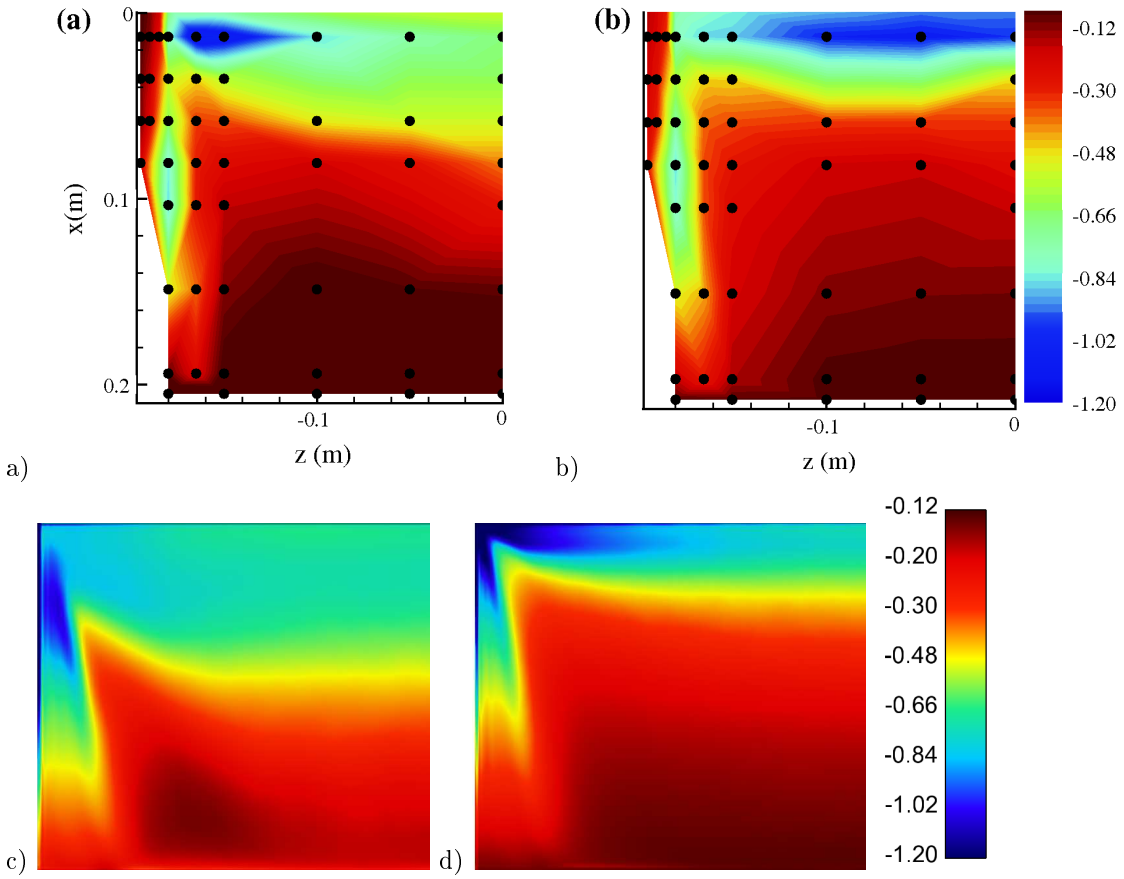

Figure 10: Comparison of the surface pressure coefficient C_p on the slanted surface of the model. a) Natural flow (experiment), b) controlled flow (experiment), c) natural flow (LES) and d) controlled flow (LES).

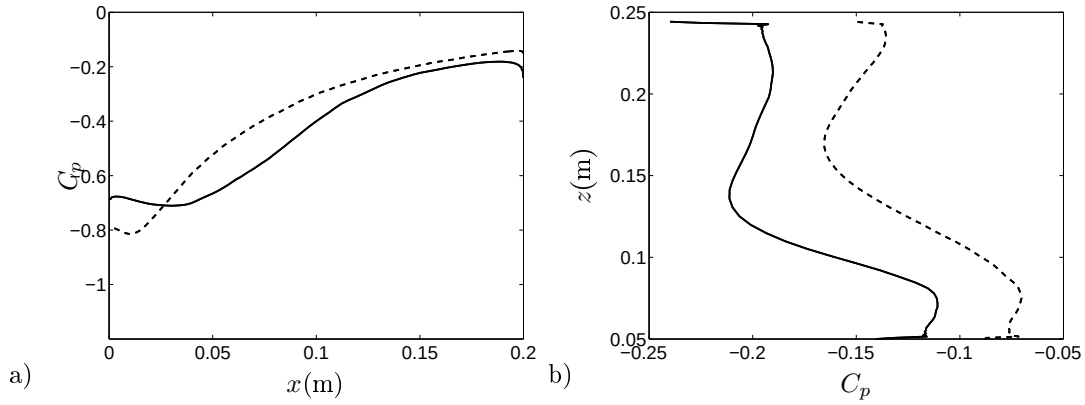

Figure 11: Comparison of the surface pressure coefficient C_p between the natural flow (solid line) and the controlled flow (dashed line) on the a) slanted surface and the b) rear face of the body. The profils are shown for $y = 0$.

natural flow). As a result of the recirculation region, the streamwise velocity distribution on the slanted surface is different in the controlled flow in the LES as compared to the experimental flow. The wall pressure distribution on the slanted surface is shown in Fig. 10. The natural flow contains two regions of low surface pressure indicating the location of the recirculation bubble and the trailing vortex. The main influence of the flow control is to decrease the size of the region of the low surface pressure under the recirculation bubble. Furthermore, in the controlled flow, the surface pressure under the separation bubble, is redistributed so that it is first decreased downstream of the position $x = 0$ and then increased. These trends in the change of C_p in the experimental observations (Fig 10a and b) are also found in the LES predictions (Fig. 10 c and d). The influence of the flow control on the surface pressure under the trailing vortices seems to be small in the experimental observations. The LES results show some increase in the surface pressure in the region of the trailing vortices as a result of the flow control. A more detailed change of the C_p is shown in Fig. 10, where a comparison between the LES of the natural and controlled flows is shown in the symmetry plane of the body ($z = 0$) for the slanted surface in Fig. 10a and for the vertical base surface in Fig. 10b.

A more detailed change of the C_p is shown in Fig. 11, where a comparison between the LES of the natural and the controlled flows is shown in the symmetry plane of the body ($z = 0$) for the slanted surface in Fig. 11a and for the vertical base surface in Fig. 11b. As previously seen in Fig. 10, the surface pressure coefficient at the beginning of the slant is lower in the natural flow than in the controlled one. The pressure recovery in the controlled flow is faster in the controlled flow, however, leading to a higher surface pressure at location $x = 0.0265$ m, which is similar to the experimental observation (Pujals et al. [1]). The influence of the flow control on the surface pressure of the vertical base in Fig. 11b is an increase of the pressure coefficient by approximately $\Delta C_p = 0.04$. These results show that the passive flow control applied here has a beneficial influence on the surface pressure on both the slanted surface and the base of the model.

The influence of the flow control on the trailing vortices was explored and is shown in Fig. 12, where the trailing vortex is followed along the slanted surface and the near wake. Figure 12a shows that the natural flow contains two regions with distinct streamwise vorticity, in the region of the recirculation region (blue) and in the trailing vortex (red). The flow control suppresses the recirculation region, indicated by the absence of the strong negative vorticity here. Furthermore, the trailing vortex is shifted up in the controlled flow. This displacement of the trailing vortex is visible all the way to the rear end of the slanted surface (Fig. 12 b). The position of the trailing vortex in the near wake (Fig. 12 c) is shifted down, and the strength of the vortex is somewhat reduced.

4.2 Vortices generated by the cylindrical roughness

The formation of the large-scale coherent streamwise streaks is illustrated in Fig. 13 as isosurfaces of the streamwise vorticity. This figure shows that the streaks are formed behind the cylinder and extend downstream on the roof all the way to the slanted surface.

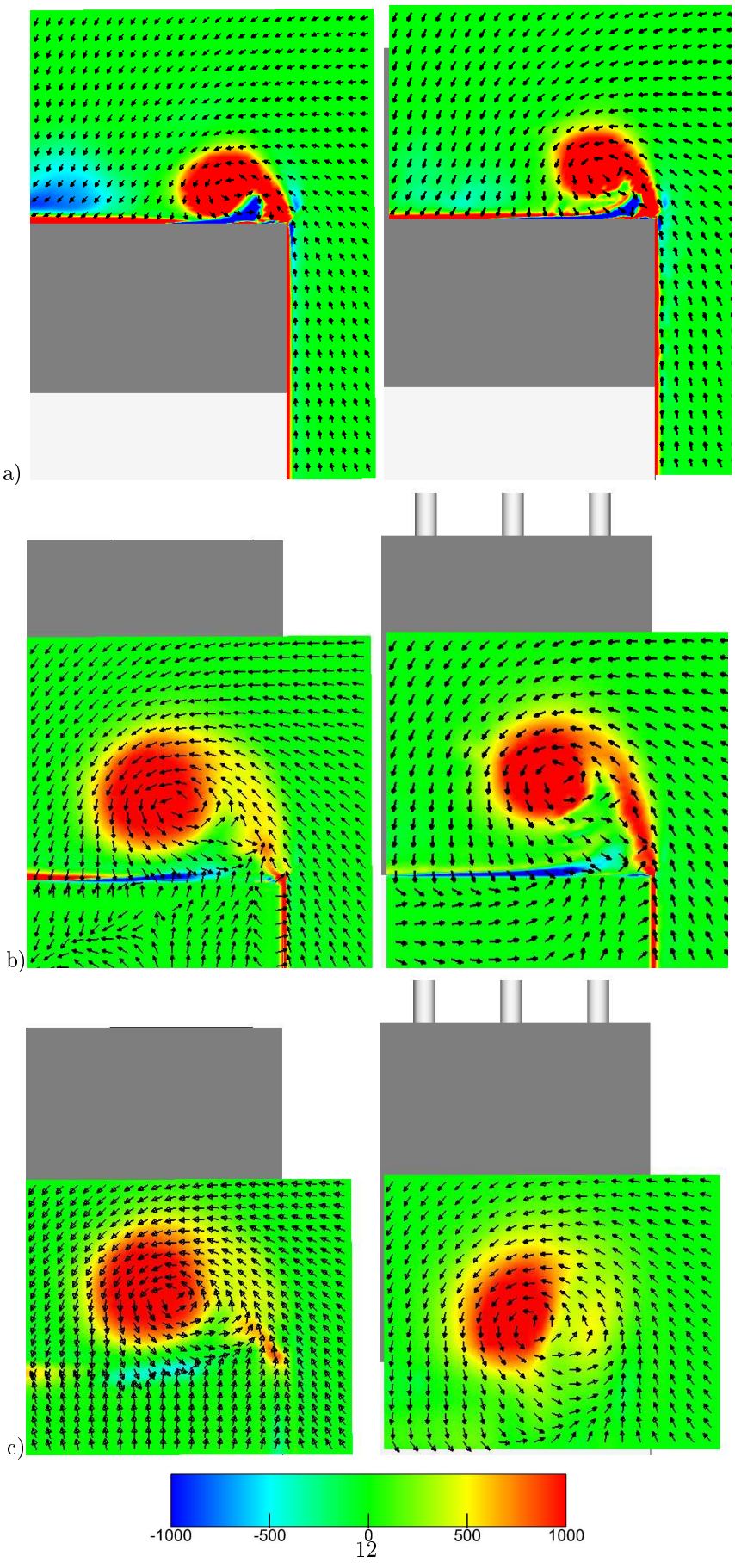

Figure 12: Planes of the streamwise vorticity component ω_x (color) and velocity vectors at locations a) $x = 0.1$m, b) $x = 0.2$m and c) $x = 0.25$m. View from behind the model. The natural and the controlled flows are shown on the left and the right sides, respectively.

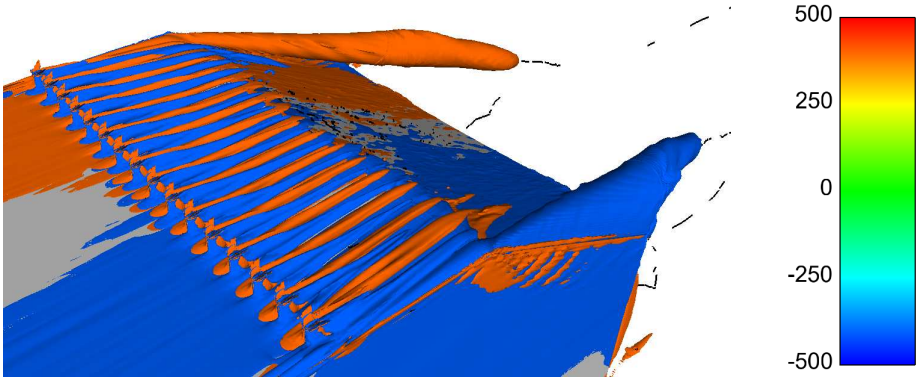

Figure 13: Large-scale coherent trailing vortices. Two iso-surfaces of the streamwise vorticity component $\omega_x = 400$ and $\omega_x = -400$. Flow is from left to right. The black lines represent the vortex cores.

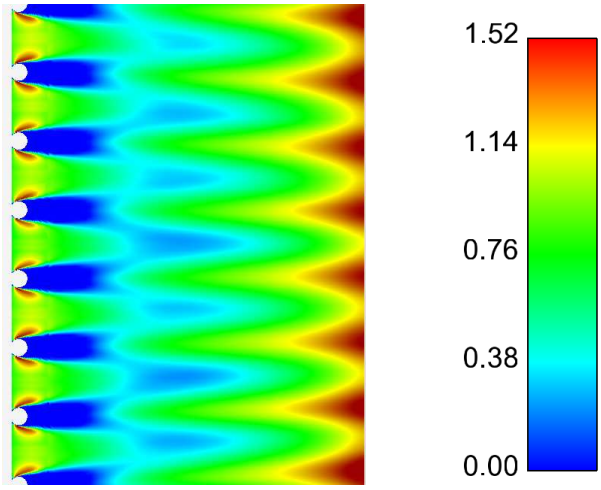

Figure 14: Large-scale coherent trailing vortices on the roof of the model 6 mm above the surface. The plane is colored with the time-averaged streamwise velocity, U/U_∞. The flow is from left to right.

Figure 14 shows a time-averaged streamwise velocity in a plane located downstream of the cylinders and 6 mm above the roof. The flow is strongly affected by the presence of the cylinders which results in high-speed (warm colors) and low-speed (cold colors) streaks.

A more detailed analysis of the streaks can be seen in Fig. 15, which shows several planes downstream of the cylinders. The combination of the streamwise vorticity component, ω_x, and the velocity vectors in these planes illustrates the structures of the vortices.

This figure shows that three different regions can be identified in the wake of the cylinders. The first region is the near wake, where the streamwise vortices are generated as shown in Figs. 15a and b. Six regions of strong vorticity are visible at location $x = -0.001$mm, showing the streamwise vortices in the near wake and the legs of the horse-shoe vortex near the ground plane. The longitudinal vortices are already visible at $x = -0.042$mm. They grow in strength in Fig. 15c, at the same time as the streamwise vortices decay. The streaks are strong at approximately $x = -0.101$mm but are no longer visible at $x = -0.111$mm.

4.3 Prediction of the active flow control

4.3.1 Global flow parameters

The global flow parameters are examined first. The drag coefficients and Strouhal number ($St = fH/U_\infty$) computed by the PANS method are compared with LES and experimental results, shown in Table 1. On the

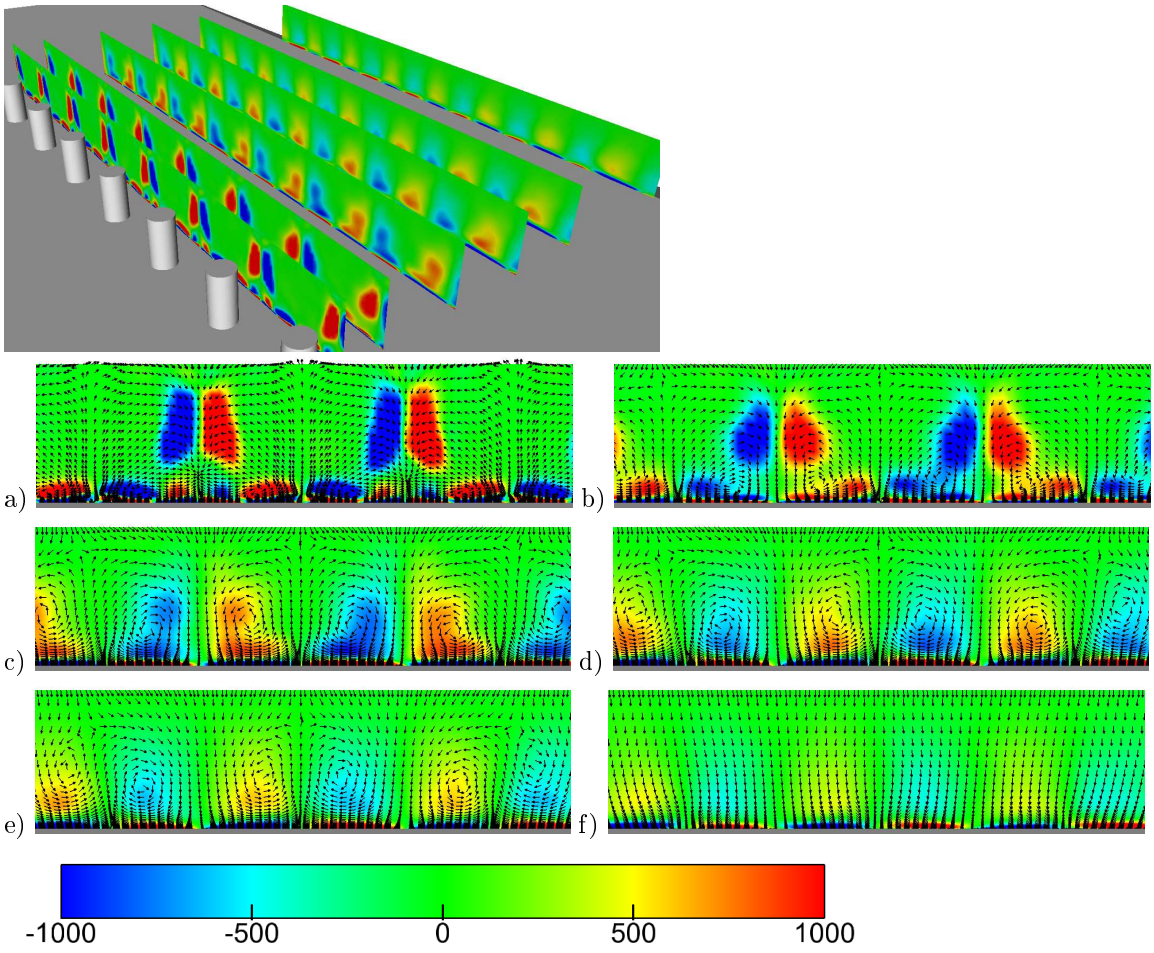

Figure 15: Planes of the streamwise vorticity, $omega_x$, at: a) $x = -0.001$mm, b) $x = -0.041$mm, c) $x = -0.061$mm, d) $x = -0.081$mm, e) $x = -0.101$mm and f) $x = -0.111$mm

Table 1: Comparisons of drag coefficients and Strouhal number. M1 means the coarse mesh with about 3.0×10^6 nodes, M2 means the medium mesh with about 5.5×10^6 nodes and M3 means the fine mesh with about 7.5×10^6 nodes. NAT means the natural case and CON means the controlled case.

	PANS -M1		PANS -M2		PANS -M3		LES study [3]		Experiment [8]	
	NAT	CON	NAT	CON	NAT	CON	NAT	CON	NAT	CON
St	0.35	0.17&0.35	0.35	0.17&0.34	0.35	0.17&0.35	0.31	0.17&0.31	0.23-0.25	-
$\bar{C}_D$	0.93	0.86	1.00	0.90	1.00	0.85	1.02	0.92	0.98	0.83
$\Delta\bar{C}_D(\%)$	-	7.5	-	10.0	-	15.0	-	9.8	-	15.3

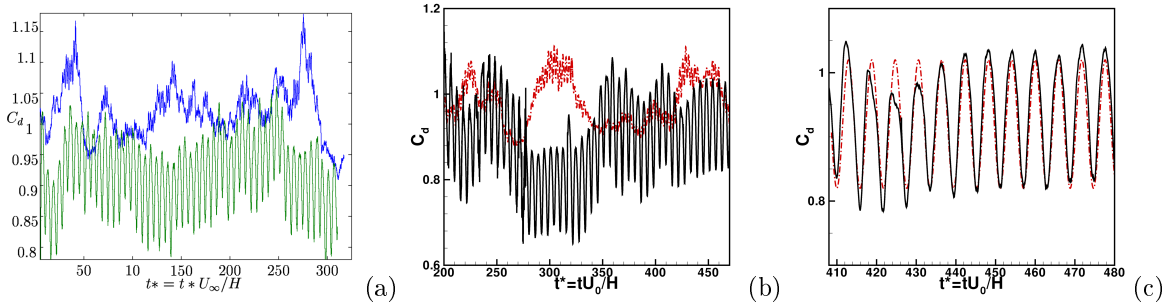

Figure 16: Time history of the drag coefficient on the medium mesh (M2): (a) previous LES study, (b) the present PANS method for the natural (upper curve) and controlled flows (lower curve), (c) partial time history of the drag coefficient for the controlled flow by the present PANS method. The dash-dotted curve shows a harmonic function with a frequency of f_A corresponding to the actuation frequency of $St_{act} = 0.17$.

fine mesh, the PANS method predicts mean drag coefficients of 1.00 and 0.85 for natural and controlled flow, respectively, i.e. a decrease of about 15% in the mean drag is obtained by flow control actuation, which is quite close to the experimental data of 15.3%. On the medium mesh, the PANS method predicts a decrease of 10% in the mean drag which is close to the previous LES result of 9.8% with the same mesh resolution. The individual drag coefficients of the natural and controlled cases by PANS on the medium and fine meshes agree well with experimental data, and all are closer to the experimental data than in previous LES studies. Overall, the PANS method better predicts results of global drag than LES on the same medium mesh. The accuracy of the drag predictions by the PANS method decreases on the coarse mesh. However, a decrease of 7.5% in the drag was still predicted. Note that the total number of nodes in the coarse mesh is about 54.5% of that of the medium mesh, which means that the coarse mesh is much coarser than the medium mesh. Considering this, the PANS method performs acceptably even on the coarse mesh. In the natural case, the PANS method exhibits a proportional behavior for predicting the drag coefficient with the mesh resolution; this is not true for the controlled case. There are two dominant frequencies of the vortex shedding in the controlled case (see the Strouhal number results in Table 1), which means the controlled flow is more complex than the natural flow. It is thus more difficult to accurately predict the controlled case than the natural case.

The time history of the drag coefficient by the PANS method on the medium mesh is shown in Fig. 16, including the results of the LES study on the same mesh [3]. It can be seen that the shapes of both curves in the present PANS model are quite similar to those in the LES study. The power spectra densities (PSD) of the drag and lift signals were computed for both the natural and the controlled case. Results of the Strouhal number in Table 1 are based on the PSD of drag signals consistent with the LES study in [3]. It can be seen from the results of the Strouhal number in Table 1 that PANS on all the three meshes predict a larger dominant frequency in the natural flow than in experiments, while they are quite close to the LES prediction.

5 Conclusion and Future Work

The aim of the present paper was to investigate the capabilities of two time-dependent numerical techniques, LES and PANS, to predict flows around generic vehicle bodies with flow control. Both passive and active flow control techniques were explored, and both pose challenges for the numerical prediction. LES is a technique that has proven to be reliable in vehicle-like bluff-body flow predictions [25, 19, 6, 26, 27, 22, 20, 23, 21]. However, as the quality of the LES prediction is strongly dependent on the resolution of the near-wall flow structures, the Reynolds number used in the LES simulation was moderate (up to approximately 4×10^5 based on the height of the body and the inlet velocity). The idea behind the development of PANS was to overcome the Reynolds number limitation. Although the PANS has been shown to be superior to the LES for some flow predictions when coarse (read "affordable") computational grids are used, the trend is not clear for general bluff body flows. The prediction of the bluff-body flows studied here is known to be challenging even without flow control. The flow around the Ahmed body with the slanted surface at 25^o has been shown to be particularly difficult to predict when the turbulence model is used (either in pure RANS simulations or hybrid RANS-LES approaches (such as DES)). Unfortunately, the PANS approach also has problems with the prediction of this flow that are probably related to the RANS modeling in the near-wall region.

The flow control processes studied in the present paper complicate the problem of flow prediction. The passive flow control devices used on the Ahmed body are bluff bodies with their own regions of separated flow. The cylindrical shape of the flow control devices results in a separation defined by the pressure gradient except on the top of the cylinders, where the separation occurs at the sharp edge. Although such flows can be predicted with both LES and PANS, there are great resolution requirements, and, having 16 such bodies in the flow, the required computer effort for good prediction becomes very large. On the other hand, the active flow control studied here aims to influence shear-layer instabilities. This is a sensitive physical process, and its prediction requires the resolution of relatively small turbulent scales. The actuation applied in the present work, consisting of periodic blowing and suction, leads to a large change in the local flow velocity in the region of actuation. The computational grids and the time steps were unchanged in the natural and the controlled flows in the present work, which led to large variation of the flow resolution in the flow regions where the boundary layers separate and form shear layers. Unfortunately, these regions are of great importance for the flow studied here. Previous work by Krajnović and Fernandes [3] showed that, despite the reduced accuracy of the actuated flow due to the usage of an identical computational grid, the LES was capable of providing an accurate prediction. The present PANS simulations show that the results are less sensitive to numerical resolution than LES. This is an encouraging result as it shows that PANS may have the capacity to overcome LES problems with overwhelming resolution requirements.

The results of the present work concerning the capabilities of the LES and PANS to predict flow controlled flows around vehicle-like bodies should be seen as initial attempts to use these techniques for flow control applications. Only LES seems to be capable of predicting the Ahmed body flow with a 25^o slanted surface. The introduction of the flow control devices substantially increases the resolution requirements, and the task of refining the computational grid and proving the convergence of the LES results for this case remain. An increase of the Reynolds number for this case to the operational speeds of ground vehicles is still geyond the reach of existing computer capabilities. The active flow control case seems to be the easier task for prediction by both LES and PANS. The reason for this is in the two-dimensionality of the geometry, leading to only two shear layers. The good news is that PANS seems to work well using rather course computational grids. It remains to be investigated wheather higher Reynolds numbers can be predicted with the present PANS approach on affordable computational grids. Furthermore, PANS simulations of fully three-dimensional geometries with active flow control remain to be tested.

Acknowledgements

The work presented here was funded by Trafikverket and the Chalmers Sustainable Transport Initiative. The authors are grateful to AVL List GmbH for providing the licenses for the AVL FIRE solver for the project. Computation time at SNIC (the Swedish National Infrastructure for Computing) at the Center for Scientific Computing at Chalmers (C3SE) is gratefully acknowledged.

References

[1] G. Pujals, S. Depardon, and C. Cossu. Drag reduction of a 3d bluff body using coherent streamwise streaks. *Experiments in Fluids*, 49:1085–1094, 2010.

[2] M. Pastoor, L. Henning, B. R. Noack, R. King, and G. Tadmor. Feedback shear layer control for bluff body drag reduction. *Journal of Fluid Mechanics*, 608:161–196, 2008.

[3] S. Krajnović and J. Fernandes. Numerical simulation of the flow around a simplified vehicle model with active flow control. *Int. J. Heat and Fluid Flow*, 32 (1):192–200, 2011.

[4] S. R. Ahmed, G. Ramm, and G. Faltin. Some salient features of the time averaged ground vehicle wake. SAE Paper 840300, 1984.

[5] H. Lienhart and S. Becker. Flow and turbulent structure in the wake of a simplified car model. SAE Paper 2003-01-0656, 2003.

[6] S. Krajnović and L. Davidson. Flow around a simplified car, part 1: Large eddy simulation. *ASME: Journal of Fluids Engineering*, 127:907–918, 2005.

[7] S. Krajnović and L. Davidson. Flow around a simplified car, part 2: Understanding the flow. *ASME: Journal of Fluids Engineering*, 127:919–928, 2005.

[8] L. Henning. *Regelung abgelöster Scherschichten durch aktive Beeinflussung. PhD thesis.* PhD thesis, Technischen Universität Berlin, Germany, 2008.

[9] B. Chaouat and R. Schiestel. A new partially integrated transport model for subgrid-scale stresses and dissipation rate for turbulent developing flows. *Physics of Fluids*, 17(6):1–19, 2005.

[10] S. Girimaji, R. Srinivasan, and E. Jeong. PANS turbulence models for seamless transition between RANS and LES: Fixed point analyses and preliminary results. In *ASME paper FEDSM2003-4336*, 2003.

[11] S. Girimaji. Partially-averaged navier-stokes model for turbulence: A reynolds-averaged navier-stokes to direct numerical simulation bridging method. *Journal of Applied Mechanics*, 73(3):413–421, 2006.

[12] S. S. Girimaji and K. S. Abdol-Hamid. Partially-averaged navierâĂŞstokes model for turbulence: implementation and validation. AIAA Paper 2005-0502, 2005.

[13] B. Basara, S. Krajnović, and S. Girimaji. Pans vs. les for computing of the flow around a 3d bluff body. In *7th International ERCOFTAC Symposium on Engineering Turbulence Modelling and Measurements*, Limassol, Cyprus, 4-6 June, 2008.

[14] B. Basara, S. Krajnović, S. Girimaji, and Z. Pavlović. Near-Wall Formulation of the Partially Averaged Navier stokes Turbulence Model. *AIAA Journal*, 49(12):December, 2011.

[15] K. Hanjalić, M. Popovac, and M. Hadžiabdić. A robust near-wall elliptic-relaxation eddy-viscosity turbulence model for cfd. *Int. J. Heat and Fluid Flow*, 25:1047–1051, 2004.

[16] P. A. Durbin. Near-wall turbulence closure modelling without damping functions. *Theoretical and Computational Fluid Dynamics*, 3:1–13, 1991.

[17] J. Smagorinsky. General circulation experiments with the primitive equations. *Monthly Weather Review*, 91(3):99–165, 1963.

[18] S. Krajnović and L. Davidson. Large eddy simulation of the flow around a bluff body. *AIAA Journal*, 40(5):927–936, 2002.

[19] S. Krajnović and L. Davidson. Numerical study of the flow around the bus-shaped body. *ASME: Journal of Fluids Engineering*, 125:500–509, 2003.

[20] S. Krajnović, A. Bengtsson, and B. Basara. Large eddy simulation investigation of the hysteresis effects in the flow around an oscillating ground vehicle. *ASME: Journal of Fluids Engineering*, 133:121103, 2011.

[21] S. Krajnović, S. Sarmast, and B. Basara. Numerical investigation of the flow around a simplified wheel in a wheelhouse. *ASME: Journal of Fluids Engineering*, 133:111001, 2011.

[22] S. Krajnović, J. Osth, and B. Basara. LES study of breakdown control of a-pillar vortex. *International Journal of Flow Control*, 2(4):237–257, 2011.

[23] J. Osth and S. Krajnović. The flow around a simplified tractor−trailer model studied by large eddy simulation. *Journal of Wind Engineering and Industrial Aerodynamics*, 102:36–47, 2012.

[24] S. Krajnović. Flow around a tall finite cylinder explored by large eddy simulation. *Journal of Fluid Mechanics*, 676:294–317, 2011.

[25] S. Krajnović. LES of flows around ground vehicles and other bluff bodies. *Philosophical Transactions of The Royal Society A*, 367 (1899):2917–2930, 2009.

[26] S. Krajnović and L. Davidson. Influence of floor motions in wind tunnels on the aerodynamics of road vehicles,. *Journal of Wind Engineering and Industrial Aerodynamics*, 93,9:677–696, 2005.

[27] H. Hemida and S. Krajnović. LES study of the influence of train nose shape on the flow structures under cross-wind conditions. *ASME: Journal of Fluids Engineering*, 130, 2008.